AMERICAN
METEOROLOGICAL
SOCIETY

Journal of Climate

The DOI for this manuscript is doi: 10.1175/2011JCLI4092.1

Seasonality of the Pacific Decadal Oscillation

HUI WANG[1,2], ARUN KUMAR[1], WANQIU WANG[1], and YAN XUE[1]

[1]*Climate Prediction Center, NCEP/NWS/NOAA, Camp Springs, Maryland*
[2]*Wyle Information Systems, McLean, Virginia*

Journal of Climate
Manuscript submitted 20 September 2010
Revised 29 January 2011 and 17 May 2011

Corresponding author address: Dr. Hui Wang, NOAA Climate Prediction Center, 5200 Auth Road, Camp Springs, MD 20746.
E-mail: hui.wang@noaa.gov

ABSTRACT

The seasonality of the Pacific decadal oscillation (PDO) is examined using North Pacific sea surface temperature (SST) in observations and in a 480-yr simulation with the National Centers for Environmental Prediction (NCEP) Climate Forecast System (CFS) coupled model. The PDO, both in observations and in the CFS, shows similar seasonality, with increasing SST variance during spring and a maximum in late spring and early summer. The vertical structure of the ocean temperature anomaly associated with the PDO in the CFS displays a significant transition from a deep to a shallow structure during late spring, consistent with the seasonal variation of the mean ocean mixed layer depth (MLD). An analysis of atmospheric surface wind and SST anomalies from the CFS simulation indicates that there is a 1-month delay in the PDO-related SST response to the atmospheric wind forcing. The results based the CFS simulation are generally consistent with observations, including both atmospheric data from the NCEP/Department of Energy (DOE) Reanalysis 2 (R2) and ocean data from the NCEP Global Ocean Data Assimilation System (GODAS). The 1-month delay together with the seasonal variation of the mean MLD tends to amplify the PDO-related SST response to the atmospheric surface wind in late spring to early summer, and leads to the maximum variability of the PDO, which is a 3-month delay from the peak phase of the surface wind in February and March.

1. Introduction

The Pacific decadal oscillation (PDO) is the leading empirical orthogonal function (EOF) of monthly mean sea surface temperature (SST) anomalies in the North Pacific (Mantua et al. 1997; Zhang et al. 1997). The causes of the PDO are the subject of many previous studies. Proposed mechanisms responsible for the spatial and temporal characteristics of the PDO include stochastic forcing of the ocean by the atmosphere (Alexander 2010), coupling of the midlatitude ocean-atmosphere system (Barnett et al. 1999), the reemergence of deep oceanic mixed layer temperature anomaly leading to a multi-year persistence of the PDO (Alexander et al. 1999), tropical forcing by the El Niño–Southern Oscillation (ENSO; Newman et al. 2003; An et al. 2007; Shakun and Shaman 2009), and the variability of the Aleutian low and Kuroshio Extension (Qiu 2003; Schneider and Cornuelle 2005), among others.

Similar to ENSO, the PDO is associated with broad impacts on global climate (Mantua and Hare 2002). However, unlike the influence of ENSO, the PDO-related precipitation and temperature anomalies in North America are not strongest in winter (Minobe 2000; Cayan et al. 2001; Hu and Huang 2009). It is also well known that tropical SST variability related to ENSO influences the PDO through the atmospheric bridge mechanism (Alexander et al. 2002). Specifically, ENSO can significantly alter the variability of the Aleutian low. The latter in turn affects the PDO. Furthermore, this "tropical-extratropical" linkage between ENSO and the PDO occurs on interannual time-scales, and is likely to follow the seasonality in the evolution of both ENSO SST anomalies in the tropical Pacific and the characteristics of tropical-extratropical teleconnection (Newman and Sardeshmukh, 1998).

The PDO can also modulate the impact of ENSO on extratropical climate (e.g., Gershunov and Barnett 1998; Wang et al. 2008; Birk et al. 2010) by altering the background mean flow (on which tropical-extratropical teleconnection depend) on decadal time-scales. Further, based on the seasonality of the PDO, such a modulation may also have a seasonality.

What factors determine the characteristic seasonal evolution of the PDO? With much focus on the low-frequency evolution of the PDO, seasonal variations in the PDO characteristics have received less attention. Diagnosis and budget analysis with oceanic models indicate that atmospheric heat flux (Dawe and Thompson 2007), the variability of the Aleutian low and anomalous advection of mean SST (Chhak et al. 2009) are important for the seasonal evolution of the PDO. However, the understanding is far from comprehensive. A better understanding of the seasonality of the PDO is important for potential improvements in our understanding of its predictability and prediction skill, its global associations, and its decadal modulation of the impact of ENSO on extratropical climate.

This study aims to characterize the seasonality of the PDO and potential mechanisms. Our hypothesis is that the PDO seasonality is dominated by the combined influence of the seasonal variations in the atmospheric forcing and oceanic mixed layer depth (MLD). Our emphasis is on the PDO evolution from spring to summer because as will be shown, there are significant changes in 1) the seasonal characteristics of the PDO, and 2) the strength of the atmospheric forcing and MLD between the two seasons, both of which play an important role in the variability of midlatitude SST (Alexander and Penland 1996).

2. Data

Our analysis is based on data from observations and a coupled model simulation. As will be shown, the spatial pattern and seasonality of the PDO are similar between observations and the coupled model simulation. Use of the model simulation allows us to investigate the seasonality of the PDO based on a longer and more consistent ocean-atmosphere model data set.

The SST used in this study includes observational data from the National Oceanic and Atmospheric Administration (NOAA) Optimum Interpolation SST (OISST) V2 (Reynolds et al. 2002), NOAA Extended Reconstructed SST (ERSST) V3b (Reynolds et al. 2007), and simulated data from the National Centers for Environmental Prediction (NCEP) Climate Forecast System (CFS; Saha et al. 2006) coupled model. The OISST is on a $1^o \times 1^o$ (latitude × longitude) grid and over 29 years from 1982 to 2010. The 29-yr period of the satellite observations may be too short to represent PDO. The ERSST, with a longer record is also employed, which is on a $2^o \times 2^o$ (latitude × longitude) grid and over 150 years from 1861 to 2010. The SST from the CFS is on a $1^o \times 2^o$ (latitude × longitude) grid. The CFS was initialized with January 1, 1981 conditions obtained from the NCEP/Department of Energy (DOE) Reanalysis 2 (R2; Kanamitsu et al. 2002) for the atmosphere and from the NCEP Global Ocean Data Assimilation System (GODAS; Behringer and Xue 2004) for the oceans. The coupled model was integrated for 500 years. The last 480 years are used in the analysis. Data from the model simulation is divided into 16 segments of 30-yr periods. Each shorter-period segment is comparable with the 29 years in the OISST, and the analysis of PDO seasonality over 16 such

realizations provides an estimate of variability in results due to sampling (as may be the case for the OISST).

The CFS is a fully coupled ocean–atmosphere–land model, and was implemented for operational seasonal forecast at NCEP in 2004. The present version of the CFS has a horizontal resolution of T62 and 64 vertical levels in the atmospheric component of the model. This dynamical forecast system has demonstrated skillful seasonal forecasts for a number of important climate phenomena, including ENSO (Wang et al. 2005; Zhang et al. 2007), the Asian-Australian monsoon (Wang et al. 2008), and the North American monsoon (Yang et al. 2009). A detailed description of model physics and an overview of CFS performance can be found in Saha et al. (2006) and Wang et al. (2010).

Oceanic and atmospheric fields from the CFS are utilized to analyze their roles in the PDO seasonal variation. Ocean temperatures (5–300 m) resolved with 26 vertical levels in the CFS are used to characterize the vertical structure of the PDO and to derive the MLD. The latter is critical to the effectiveness of SST response to atmospheric forcing (Alexander and Penland 1996). The MLD is estimated as the depth at which the temperature change from the ocean surface is 0.5 ^{o}C (Monterey and Levitus 1997). The atmospheric field from the CFS is inferred from the 1000-hPa wind on a $2.5^{o} \times 2.5^{o}$ (latitude × longitude) grid. The results based on the CFS simulation are compared to ocean temperature and 1000-hPa wind at the same resolutions from the GODAS and R2, respectively, for the period from 1982 to 2010. Surface fluxes, including latent, sensible, long wave, short wave, and Ekman heat transport from the CFS simulation are also employed to illustrate their seasonal variations with the PDO. The contribution to change in surface heat flux due to Ekman transport is estimated using zonal and meridional

surface wind stress from the CFS outputs, as well as zonal and meridional SST gradients derived from the CFS (e.g., Alexander and Scott 2008). All data are monthly means.

The PDO is identified as the first EOF of North Pacific SST between 20°N and 65°N based on the covariance matrix of the SST anomalies. Similar to Mantua et al. (1997) and Zhang et al. (1997), the global mean SST anomaly is removed prior to the EOF analysis for the PDO, to suppress the influence of the trend of global mean SST. The spatial structure of the PDO in the CFS is the ensemble mean of the 16 different realizations of the first EOF mode of North Pacific SST based on the individual 30-yr long segments.

3. Results

a. Seasonality of the PDO

Figures 1a, 1b, and 1c show the spatial patterns of SST associated with the first EOF of monthly mean SST anomalies over the North Pacific in the OISST and ERSST data sets and the CFS simulation, respectively. This mode accounts for 23% of North Pacific SST variance in both the OISST and ERSST, and on average 21% in the CFS simulation. To some extent the PDO pattern is similar to the ENSO pattern but with higher loading in the North Pacific. The pattern correlation coefficient between the PDO in the observations and that in the CFS ensemble mean is 0.88 and 0.91 for the OISST and ERSST, respectively. The average correlation coefficient between the observations and 16 individual 30-yr segments is 0.81 (OISST) and 0.84 (ERSST).

We note that there might be nonstationarity (or variability due to sampling) in the structure of the PDO. As displayed in Fig. 1, the PDO pattern in the OISST (Fig. 1a) has

more connection with SST variability in the western tropical Pacific than the ERSST and CFS (Figs. 1b and 1c). A closer inspection reveals that similar connection between the PDO and SST in the western tropical Pacific can also be found in the ERSST when using most recent 30-yr data, and also in some individual CFS 30-yr segments. This suggests that the difference in the PDO structure between the OISST and ERSST or CFS may be due to sampling, and the short period of the OISST analysis.

The seasonality of the PDO, both in the observations and the CFS, is quantified by the distribution of the fraction (%) of total SST variance explained by the principal component (PC) time series over 12 calendar months, as shown in Fig. 1d. It is a measure of the seasonal variation of the amplitude of the PDO pattern. The amplitude of the PDO in the OISST and ERSST increases from winter to spring, reaches peak values in May and June, and then declines during summer, with a secondary maximum in fall. The relatively strong variance in summer and weak variance in winter are consistent with the finding of Zhang et al. (1998). For comparison, the seasonality based on the PDO index (Mantua et al. 1997) for 1900–2010 (available at http://jisao.washington.edu/pdo /PDO.latest) is also plotted in Fig. 1d, which was derived from the leading PC of monthly North Pacific SST using the UK Meteorological Office Historical SST data (Parker et al. 1995) for 1900–81 and the OISST for 1982–2010. This particular PDO index shows peak variability in June and July. However, it also shows strong variability in December–February that is not found in the OISST and ERSST. The difference may be due to different SST datasets.

The PDO of the CFS ensemble mean displays a seasonality with a peak in June, with relatively higher variability in summer and lower variability in winter and fall. The

peaks of the PDO variability in individual members vary from May to July. Overall, the seasonal distribution of the percentage variance for the PDO in the observations is well within the spread of 16 CFS ensemble members, except for the Mantua et al. (1997) PDO index in May and June.

Figure 1 suggests that both the spatial pattern and seasonality of the PDO in the CFS resemble those in the 150-yr ERSST more than those in the 29-yr OISST. That these features are simulated reasonably well in the CFS coupled integration allows us to use the data over a 480-yr period for further analysis. The following analysis focuses on the ensemble mean of 16 30-yr CFS coupled runs from months of January to August and comparisons with the observations, including the 29-yr (1982–2010) GODAS data, OISST, and R2 reanalysis data.

The seasonality in the amplitude of the PDO is also reflected in the vertical structure of ocean temperature anomalies associated with the PDO. Figure 2 shows the depth–longitude cross-section of the PDO-related monthly mean ocean temperature anomalies at 37^{o}N from January to August and the correlation between ocean temperature and the PC time series in the CFS. The anomalies are obtained by regressing monthly mean ocean temperature anomalies onto the PC time series of each 30-yr segment for each calendar month and then averaging regression patterns over the 16 such regression patterns. The correlation coefficients are also averaged over 16 individual 30-yr segments. Latitude 37^{o}N is the location at which the PDO SST anomaly has the largest amplitude (Fig. 1).

Figure 2 indicates that colder ocean temperature anomalies greater than 0.4^{o}C penetrate to the depth of about 150 m during winter (January and February). In March

and April the cold temperature anomalies can reach deeper layers over 250 m. In late spring, there is an abrupt decrease in the depth of the temperature anomalies colder than 0.4^{o}C. These anomalies are confined above 150 m in May, and become progressively shallower during summer.

Near the ocean surface, temperature anomalies also display strong seasonal variation (Fig. 2), consistent with the seasonality of the PDO shown in Fig. 1d. In January and February the cold temperature anomalies are relatively weak. During March and April the amplitude of the anomalies near the dateline starts to increase. The colder anomalies are zonally widespread at the surface in May and June. The correlation coefficient between the ocean temperature and the PC time series generally exceeds –0.5 in the regions with cold temperature anomalies great than 0.4 ^{o}C. These results suggest that the seasonal variation of the PDO is closely related to the seasonal changes in the vertical structure of the ocean temperature anomalies underneath.

Similar composite and correlation analyses are also performed for ocean temperature from the 29-yr GODAS data against the leading PC of the OISST in the North Pacific, and are shown in Fig. 3. Despite much shallower temperature anomalies during March and April in the GODAS data, the seasonal changes in the vertical structure of the ocean temperature anomalies associated with the PDO in the CFS (Fig. 2) resemble those in the GODAS (Fig. 3).

b. Explaining PDO seasonality: The role of seasonal variations of the MLD and atmospheric forcing

The ocean mixed layer plays an important role in the reemergence of SST anomalies in the North Pacific (Alexander et al. 1999; Deser et al. 2003) and SST changes associated with the PDO (Carton et al. 2008). In this section we show that the mean seasonal cycle of the MLD is also important in determining the timing of the maximum variability of the PDO.

Figure 4 shows the 16-member ensemble mean of 30-yr climatological MLD from January to August derived from the 480-yr CFS coupled simulation. The seasonal variation of the mixed layer is characterized by deep MLD in winter and early spring and shallow MLD in May and summer. The MLD experiences a sharp decrease from more than 100 m in April to less than 50 m in May over most of the North Pacific. The seasonal change in the vertical structure of the ocean temperature anomalies associated with the PDO (Fig. 2) exhibits similar sharp decrease in the depth of the temperature anomalies from April to May and likely follows the seasonal variation of the MLD.

The transition from a deep to shallow mixed layer during late spring is also observed in 29-yr climatological MLD in the GODAS data shown in Fig. 5. Compared to the GODAS data, the climatological MLD in the CFS is slightly deeper between 25^{o}N and 40^{o}N and north of 50^{o}N, and slightly shallower between 40^{o}N and 50^{o}N during January through April. Overall, the observed seasonal variation of the mean MLD is well simulated in the CFS.

Previous studies have also suggested that atmospheric surface wind is likely responsible for the evolution of PDO-related SST anomalies (e.g., Newman et al. 2003; Miller et al. 2004; Carton et al. 2008). To explore the contribution of surface wind forcing in generating PDO seasonality, EOF analysis is performed for 1000-hPa zonal

wind over the North Pacific region to identify the dominant mode of the atmospheric circulation variability. Figure 6 shows the regression patterns of 1000-hPa wind anomaly for individual months from January to August reconstructed based on the first EOF of 1000-hPa zonal wind together with the SST anomaly reconstructed based on the leading EOF of the North Pacific SST (Fig. 1c) in the CFS.

The surface wind exhibits a basinwide cyclonic circulation over the North Pacific associated with the variability of the Aleutian low. The wind pattern is very similar to that of Chhak et al. (2009) associated with the PDO. The budget analysis in Chhak et al. (2009) suggests that anomalous horizontal advection of mean SST by anomalous Ekman transport contributes primarily to the PDO-related SST pattern. In addition, the distribution of the surface wind in Fig. 6 can also be used to infer partially the wind-driven SST anomalies related to the PDO. For example, southerly and southeasterly wind anomalies along the west coast of North America and over the Gulf of Alaska induce an onshore Ekman transport that suppresses upwelling and warms the ocean mixed layer. In the central North Pacific to the south of 40^{o}N, westerly wind anomalies cool the ocean surface by increasing evaporation and heat flux from the ocean to the atmosphere (Cayan 1992a,b). Overall, both the warm and cold SST anomalies in the North Pacific are dynamically consistent with the surface wind pattern, indicating the PDO-related SST anomalies are likely driven by the dominant mode of the atmospheric circulation. It is noted also that the surface wind anomalies are strongest in February and March, whereas the SST anomalies are strongest in May and June.

Figure 7 shows the reconstructed 1000-hPa wind and SST anomalies associated with their corresponding leading EOFs using the 29-yr (1982–2010) 1000-hPa wind from

R2 and the OISST data. The pattern correlation coefficient for the first EOF of 1000-hPa zonal wind between the CFS ensemble mean and R2 is 0.98. The SST anomalies are generally stronger in the observations (Fig. 7) than in the CFS (Fig. 6), with more cold SST anomalies in the western subtropical North Pacific and warm SST anomalies in the eastern subtropics. In addition, as compared to the observations, the center of maximum cold SST anomalies in the CFS is shifted towards the west along 40^{o}N. This is probably a systematic bias of the CFS in representing the PDO spatial pattern. Overall, both the spatial distribution of wind and SST anomalies and their seasonal variation of the intensity of these anomalies in the CFS (Fig. 6) are consistent with the observations (Fig. 7).

The cause and effect relationship between the surface wind and SST anomalies is further investigated from the lead and lag correlation between the two PC time series of the first EOF of the 1000-hPa zonal wind and SST anomalies, as shown in Fig. 8, for both the CFS and observations. Significant correlations are found when the zonal wind leads the SST up to two months, but correlations are weak when the zonal wind lags the SST. The strongest correlation occurs for the zonal wind leading the SST by one month. The results imply that the time scale for the SST response to atmospheric wind forcing is about one month, consistent with the finding of Deser and Timlin (1997) that the time scale for mid-latitude ocean mixed layer in response to atmospheric stochastic forcing is approximately 2–3 weeks based on the analysis of weekly data.

To illustrate the importance of the interaction between the atmospheric forcing and the MLD on the seasonality of the PDO, shown in Figs. 9a and 9b are the seasonal variation of area-averaged monthly 1000-hPa zonal wind variance associated with the

first EOF of the 1000-hPa zonal wind and the evolution of the MLD over the North Pacific domain. The surface zonal wind in the CFS displays strong seasonality with the largest variability in February and March consistent with the large wind anomaly in these two months (Fig. 6). The atmospheric forcing is thus strong in February and March and weak in summer. The variability of surface zonal wind in the observations exhibits quite similar seasonal variation. It is stronger than in the CFS during November through January and weaker during February through October, with a peak in February. The MLD in both the observation and CFS also shows a similar seasonality with the deepest depth in February or March and shallowest in summer.

Variations in the surface wind forcing alone clearly cannot explain the peak of the PDO variability in May and June. Since it is the mixed layer in the upper ocean that directly responds to the atmospheric forcing, the MLD is also expected to play an important role in determining the effectiveness of SST response to the atmospheric forcing. To illustrate this, Fig. 9c shows the seasonal variation of the square root of the zonal wind variance divided by the MLD. The square root of the zonal wind variance denotes the amplitude of the zonal wind anomaly and thus the amplitude of atmospheric forcing. As divided by the MLD, the value is approximately proportional to the forcing per unit mass for the mixed layer over which the influence of atmospheric forcing gets distributed and affects the SST anomaly. Given that it takes about one month for the SST to respond to the atmospheric forcing, the values plotted in Fig. 9c for month N are obtained by using the MLD in month N and the zonal wind variance in previous month N–1. The rate of the zonal wind variance square root to the MLD in the CFS peaks in June as the PDO variability in Fig. 1d. This implies that the 1-month time scale for the

SST to respond to the atmospheric forcing, shallow MLD in summer, and relatively strong atmospheric forcing in spring, are critical to the timing of the maximum variability of the PDO in late spring and early summer. It is interesting to note that the rate for the observations in Fig. 9c peaks in May and June, consistent with the largest PDO variability in the OISST in the same months (Fig. 1d).

The mechanism proposed in this study may not work for explaining the relative peak in the variability of the PDO in the fall season (Fig. 1d). There are many other factors that may control the seasonality of the PDO, including the tropical influence related to the ENSO and seasonal variation of surface fluxes. To investigate the influence of variation in surface heat fluxes, Fig. 10 shows the seasonal change in monthly mean variance averaged over the North Pacific associated with the PC time series of the PDO in the CFS, including latent and sensible heat fluxes, net long wave and short wave radiation fluxes, and heat flux due to Ekman heat transport. Both the latent and sensible heat fluxes (Figs. 10a and 10b) are characterized by maximum variance in February and March, consistent with the largest variance of surface wind in the same months (Fig. 9a). The variance of these fluxes is low in summer, but increases again during fall. Thus, these surface heat fluxes could become increasingly important in determining the variability of the PDO during fall. For subsequent winter when MLD is largest, large variations in heat flux may not contribute to PDO variability.

The variance of long wave and short wave radiation fluxes also displays a distinctive seasonality (Fig. 10c). The seasonal change in variance of long wave flux is relatively small (note a different scale in Fig. 10c). Unlike other surface fluxes, the variance of short wave flux exhibits peaks in April–July, with values comparable to latent

heat flux. This indicates that short wave radiation in late spring and early summer could contribute more to the variability of the PDO than in other seasons. Norris et al. (1998) found that summertime low clouds tend to be negatively correlated with local SST in the North Pacific because changes in cloudiness can significantly affect surface short wave radiation flux. They also found a strong link between cloudiness and the leading EOF of sea level pressure. The latter is likely tied to the variability of the Aleutian low and the related surface wind shown in Figs. 6 and 7. Nevertheless, the seasonal change in the variance of net surface heat flux (not shown) is dominated by latent and sensible heat fluxes.

The seasonal change in the variance of surface heat flux associated with the Ekman transport (Fig. 10d) is stronger than latent and sensible heat flux (Figs. 10a and 10b). The variance of the Ekman heat flux in the CFS is also greater than in R2, especially in February and March, consistent with the corresponding 1000-hPa zonal wind variance (Fig. 9a). It has been noted earlier that oceanic entrainment related to Ekman pumping could influence the variability of the PDO in fall (Park et al. 2006). Figure 10 also suggests that the maximum variability of the PDO in late spring and early summer is largely determined by the seasonal changes in the variance of Ekman heat flux, latent and sensible heat fluxes, and the seasonal variation of the mean MLD. All of these fluxes are closely related to the atmospheric surface wind.

4. Summary

The seasonality of the PDO has been examined in this study using both the OISST and the ERSST data and a 480-yr CFS coupled simulation with particular emphasis on

the seasonal variation of the amplitude of the PDO from spring to summer. The PDO as derived from an EOF analysis of the observational data displays strong seasonality with the peak variability in May and June. The PDO in the CFS coupled simulation shows the similar spatial pattern and seasonality. The vertical structure of ocean temperature anomalies associated with the PDO is documented using the 480-yr simulation with the CFS. The PDO-related temperature anomalies are deeper (250–300 m) in spring and shallower (50–100 m) in summer. There is a notable change in the vertical depth of the temperature anomaly that varies from about 250 m in April to 100 m in May. This rapid change of the depth of the temperature anomalies is highly consistent with the seasonal variation of the mean MLD that changes rapidly from about 100–300 m in April to about 50 m in May. Such seasonal variations of the PDO-related ocean temperature anomalies and climatological MLD from spring to summer are also observed in the 29-yr NCEP GOADS data.

The EOF analysis is also applied to the 1000-hPa zonal wind from both the CFS simulation and the NCEP/DOE Reanalysis 2 (R2) to objectively identify the dominant mode of the atmospheric variability, which is characterized by a basinwide cyclonic circulation over the North Pacific. The amplitude or the variance accounted for by the first EOF has a strong seasonality with a maximum in February and March. A comparison of the EOF patterns of the surface wind and SST anomalies indicates that the PDO is partially a response to the surface wind. A lag correlation between the PC time series of the zonal wind and North Pacific SST suggests that the SST responds to the surface wind in about one month. Our analysis indicates that both the seasonal variations of surface wind variability and the mean MLD, combined with the 1-month delay of the

SST response to the surface wind lead to the peak variability of the PDO in May and June.

The results presented in this study suggest that the seasonality of the PDO does not just follow the seasonal change of the surface wind variability, but is also strongly modulated by the seasonal variation of the mean MLD. Strong surface wind variability in early spring is responsible for the concurrent increase of PDO variability. As a remarkable decrease in the MLD occurs from April to May, a relatively weak surface wind anomaly may induce a large ocean temperature anomaly over a shallower mixed layer due to the decoupling between the shallow mixed layer and the deeper ocean. Therefore, sufficient but not necessarily the strongest surface wind forcing and a very shallow MLD work together and lead to the largest PDO variability in May and June.

There are other processes that may affect the seasonality of the PDO, including the seasonal variations of solar radiation, clouds, oceanic entrainment, mean SST and associated mean SST gradient in the North Pacific (e.g., Norris et al. 1998; Park et al. 2006; Chhak et al. 2009). The variability of tropical Pacific SST also influences the PDO (e.g., Evans et al. 2001). The contribution of ENSO to the variability of oceanic signature of the PDO, however, is difficult of untangle from the analysis of observations or the coupled simulations with tropical ENSO variations. Another set of coupled model simulations where tropical SST variability is forced to follow the climatological seasonal cycle (and ENSO SST variability, and its influence on the extratropical SST variability via the atmospheric bridge mechanism is suppressed) may help isolate the contribution of ENSO on the PDO related SST variations. Also, further observational and modeling studies, including a quantitative analysis of mixed layer heat budget (e.g., Huang et al.

2011), may advance the understanding of the forcing mechanisms for the seasonality of the PDO.

Acknowledgments. This work was supported by the NOAA Climate Test Bed (CTB) Program. We thank Drs. Zeng-Zhen Hu, Caihong Wen, and Scott J. Weaver; three anonymous reviewers, and the editor for their insightful and constructive comments and suggestions.

REFERENCES

Alexander, M. A., 2010: Extratropical air-sea interaction, SST variability and the Pacific decadal Oscillation (PDO). *Climate Dynamics: Why does Climate Vary*, Ed. D. Sun and F. Bryan, AGU Monograph, in press.

Alexander, M. A., I. Blade, M. Newman, J. R. Lanzante, N.-C. Lau, and J. D. Scott, 2002: The atmospheric bridge: The influence of ENSO teleconnections on air-sea interaction over the global oceans. *J. Climate*, **15,** 2205–2231.

Alexander, M. A., C. Deser, and M. S. Timlin, 1999: The reemergence of SST anomalies in the North Pacific Ocean. *J. Climate*, **12,** 2419 – 2433.

Alexander, M. A., and C. Penland, 1996: Variability in a mixed layer ocean model driven by stochastic atmospheric forcing. *J. Climate*, **9,** 2424–2442.

Alexander, M. A., and J. D. Scott, 2008: The role of Ekman ocean heat transport in the Northern Hemisphere response to ENSO. *J. Climate*, **21,** 5688–5707.

An, S.-I., J.-S. Kug, A. Timmermann, I.-S. Kang, and O. Timm, 2007: The influence of ENSO on the generation of decadal variability in the North Pacific. *J. Climate*, **20,** 667–680.

Barnett, T. P., D. W. Pierce, R. Saravanan, N. Schneider, D. Dommenfet, and M. Latif, 1999: Origins of the midlatitude Pacific decadal variability. *Geophys. Res. Lett.*, **26,** 1453–1456.

Behringer, D. W., and Y. Xue, 2004: Evaluation of the global ocean data assimilation system at NCEP: The Pacific Ocean. *Eighth Symposium on Integrated Observing and Assimilation System for Atmosphere*, Oceans and Land Surface, AMS 84th Annual Meeting, Seattle, Washington, 11–15 January 2004.

Birk, K., A. R. Lupo, P. Guinan, and C. E. Barbieri, 2010: The interannual variability of Midwestern temperatures and precipitation as related to the ENSO and PDO. *Atmósfera*, **23,** 95–128.

Carton, J. A., S. A. Grodsky, and H. Liu, 2008: Variability of the ocean mixed layer, 1960–2004. *J. Climate*, **21,** 1029–1047.

Cayan, D. R., 1992a: Latent and sensible heat flux anomalies over the northern oceans: The connection to monthly atmospheric circulation. *J. Climate*, **5,** 354–369.

Cayan, D. R., 1992b: Latent and sensible heat flux anomalies over the northern oceans: Driving the sea surface temperature. *J. Phys. Oceanogr.*, **22,** 859–879.

Cayan, D. R., A. A. Kammerdiener, M. D. Dettinger, J. M. Caprio, and D. H. Peterson, 2001: Changes in the onset of spring in western United States. *Bull. Amer. Meteor. Sco.*, **82,** 399–415.

Chhak, K. C., E. D. Lorenzo, N. Schneider, and P. F. Cummins, 2009: Forcing of low-frequency ocean variability in the northeast Pacific. *J. Climate*, **22,** 1255–1276.

Dawe, J. T., and L. Thompson, 2007: PDO-related heat and temperature budget changes in a model of the North Pacific. *J. Climate*, **20,** 2092–2108.

Deser, C, M. A. Alexander, and M. S. Timlin, 2003: Understanding the persistence of sea surface temperature anomalies in midlatitudes. *J. Climate*, **16,** 57–72.

Deser, C, and M. S. Timlin, 1997: Atmosphere – ocean interaction on weekly timescales in the North Atlantic and Pacific. *J. Climate*, **10,** 393–408.

Evans, M. N., M. A. Cane, D. P. Schrag, A. Kaplan, B. K. Linsley, R. Villalba, and G. M. Wellington, 2001: Support for tropically-driven Pacific decadal variability based on paleoproxy evidence. *Geophys. Res. Lett.*, **28,** 3689–3692.

Gershunov, A. and T. P. Barnett, 1998: Interdecadal modulation of ENSO teleconnections. *Bull. Amer. Meteor. Soc*, **79**, 2715–2725.

Hu, Z.-Z., and B. Huang, 2009: Interferential impact of ENSO and PDO on dry and wet conditions in the U.S. Great Plains. *J. Climate*, **22,** 6047–6065.

Huang, B., Y. Xue, D. Zhang, A. Kumar, and M. J. McPhaden, 2010: The NCEP GODAS ocean analysis of the tropical Pacific mixed layer heat budget on seasonal to interannual time scales. *J. Climate*, in press.

Kanamitsu, M., W. Ebisuzaki, J. Woollen, S.-K. Yang, J. J. Hnilo, M. Fiorino, and G. L. Potter, 2002: NCEP–DOE AMIP-II Reanalysis (R-2). *Bull. Amer. Meteor. Soc.*, **83,** 1631–1643.

Mantua, N. J., and S. R. Hare: The Pacific decadal oscillation. *J. Oceanogr.*, **58,** 35–44.

Mantua, N. J., S. R. Hare, Y. Zhang, J. M. Wallace, and R. Francis, 1997: A Pacific interdecadal climate oscillation with impacts on salmon production. *Bull. Amer. Meteor. Soc.*, **78,** 1069–1079.

Miller, A. J., F. Chai, S. Chiba, J. R. Moisan, and D. J. Neilson, 2004: Decadal-scale climate and Ecosystem interactions in the North Pacific Ocean. *J. Oceanogr.*, **60,** 163–188.

Minobe, S., 2000: Spatio-temporal structure of the pentadecadal variability over the North Pacific. *Prog. Oceanogr.*, **47,** 381–408.

Monterey, G., and S. Levitus, 1997: Seasonal variability of mixed layer depth for the world ocean. *NOAA Atlas NESDIS*, **14,** U.S. Gov. Printing Office, Washington, D.C., 96pp.

Newman, M. E., and P. D. Sardeshmukh, 1998: The impact of the annual cycle on the North Pacific/North American response to remote low-frequency forcing. *J. Atmos. Sci.*, **55,** 1336–1353.

Newman, M., G. P. Compo, and M. A. Alexander, 2003: ENSO-forced variability of the Pacific decadal oscillation. *J. Climate*, **16,** 3853–3857.

Norris, J. R., Y. Zhang, and J. M. Wallace, 1998: Role of low clouds in summertime atmosphere-ocean interactions over the North Pacific. *J. Climate*, **11,** 2482–2490.

Park, S., M. A. Alexander, and C. Deser, 2006: The impact of cloud radiative feedback, remote ENSO forcing, and entrainment on the persistence of North Pacific sea surface temperature anomalies. *J. Climate*, **19,** 6243–6261.

Parker, D. E., C. K. Folland, and M. Jackson, 1995: Marine surface temperature: Observed variations and data requirements. *Climate Change*, **31,** 559–600.

Qiu, B., 2003: Kuroshio Extension variability and forcing of the Pacific decadal oscillation: Responses and potential feedback. *J. Phys. Oceanogr.*, **33,** 2465–2482.

Reynolds, R. W., N. A. Rayner, T. M. Smith, D. C. Stokes, and W. Wang, 2002: An improved in situ and satellite SST analysis for climate. *J. Climate*, **15,** 1609–1625.

Saha, S., and Coauthors, 2006: The NCEP Climate Forecast System. *J. Climate*, **19,** 3483–3517.

Schneider, N., and B. D. Cornuelle, 2005: The forcing of the Pacific decadal oscillation. *J. Climate*, **18,** 4355–4373.

Shakun, J., and J. Shaman, 2009: Tropical origins of North and South Pacific decadal variability. *Geophys. Res. Lett.*, **36,** L19711, doi:10.1029/2009GL040313.

Smith, T. M., R. W. Reynolds, T. C. Peterson, and J. Lawrimore, 2008: Improvements to NOAA's historical merged land–ocean surface temperature analysis (1880–2006). *J. Climate*, **21,** 2283–2296.

Wang, B., and Coauthors, 2008: How accurately do coupled climate models predict the Asian-Australian monsoon interannual variability? *Climate Dyn*., **30,** 605–619.

Wang, L., W. Chen, and R. Huang, 2008: Interdecadal modulation of PDO on the impact of ENSO on the east Asian winter monsoon. *Geophys. Res. Lett.*, **35,** L20702, doi:10.1029/2008GL035287.

Wang, W., M. Chen, and A. Kumar, 2010: An assessment of the CFS real-time seasonal forecasts. *Wea. Forecasting*, 950–969.

Wang, W., S. Saha, H.-L. Pan, S. Nadiga, and G. White, 2005: Simulation of ENSO in the new NCEP Coupled Forecast System Model (CFS03). *Mon. Wea. Rev.*, **133,** 1574–1593.

Yang, S., Y. Jiang, D. Zheng, R. W. Higgins, Q. Zhang, V. E. Kousky, and M. Wen, 2009: Variations of U.S. regional precipitation and simulations by the NCEP CFS: Focus on the Southwest. *J. Climate*, **22,** 3211–3231.

Zhang, Q., A. Kumar, Y. Xue, W. Wang, and F.-F. Jin, 2007: Analysis of the ENSO cycle in the NCEP Coupled Forecast Model. *J. Climate*, **20,** 1265–1284.

Zhang, Y., J. R. Norris, and J. M. Wallace, 1998: Seasonality of large-scale atmosphere–ocean interaction over the North Pacific. *J. Climate*, **11,** 2473–2481.

Zhang, Y., J. M. Wallace, and D. S. Battisti, 1997: ENSO-like interdecadal variability. *J. Climate*, **10,** 1004–1020.

Figure Captions

Fig. 1. Spatial patterns of SST associated with the first EOF of monthly mean SST over the North Pacific (20°N–65°N, 125°E–100°W) based on the (a) OISST data during 1982–2010, (b) ERSST during 1861–2010, and (c) the ensemble average of 16 leading EOFs for individual 30-yr segments from the 480-year CFS coupled run, and (d) seasonal distribution of the percentage variance of PC time series with red for the OISST, green for the ERSST, orange for the PDO index (1900–2010; Mantua et al. 1997), light blue for 16 individual 30-yr segments, and black for the 16-member ensemble. The spatial patterns in (a,b,c) are displayed in correlation maps in which the monthly mean SST anomalies at each grid point are correlated with the corresponding PC time series.

Fig. 2. PDO-related monthly ocean temperature anomalies (shading, °C) and correlation (contour) with the PDO PC time series at 37°N across the North Pacific in the CFS. The anomalies are obtained by regressing ocean temperature anomaly vs. the PC time series of the first EOF of North Pacific SST in individual 30-yr segments. The anomalies are based on the ensemble average of 16 members and are associated with one standard deviation fluctuations in the PC time series for months from January to August. The correlation coefficients are also based on the ensemble average of the 16 members. Contours are ±0.3, ±0.5, and ±0.7 with negative contours dashed.

Fig. 3. Same as in Fig. 2, but based on 29-yr (1982–2010) ocean temperature from the GODAS and the first EOF of North Pacific SST from the OISST.

Fig. 4. Monthly climatology of the mixed layer depth (MLD; m) in the North Pacific derived from the CFS coupled run ensemble averaged over 16 30-yr segments for months from January to August.

Fig. 5. Same as in Fig. 4, but based on 29-yr (1982 – 2010) GODAS data.

Fig. 6. Regression patterns of 1000-hPa wind (vectors; m s^{-1}) and SST (shadings, °C) anomalies in the CFS associated with one standard deviation departures of the PC

time series of the first EOF of 1000-hPa zonal wind and SST anomalies over the North Pacific, respectively. The regressions are performed over the 30-yr period and all months, but one standard deviation values of the PC time series are calculated for individual months from January to August. The results are shown based on 16-member ensemble.

Fig. 7. Same as in Fig. 6, but based on 29-yr (1982 – 2010) 1000-hPa wind from R2 and OISST.

Fig. 8. Lag correlations between the PC time series of the first EOF of monthly 1000-hPa zonal wind and SST over the North Pacific in the CFS coupled run for each 30-yr period (light blue) and ensemble average (black) of the 16 correlation coefficients at different lags and those using 29-yr 1000-hPa zoanl wind from R2 and OISST (red). Negative (positive) lag means the 1000-hPa zonal wind leading (lagging) the SST.

Fig. 9. Seasonal variations of area-averaged (20^{o}–65^{o}N, 125^{o}E–120^{o}W) (a) monthly mean variance of the 1000-hPa zonal wind anomaly associated with the first EOF, (b) climatological MLD, and (c) square root of the zonal wind variance in month N–1 divided by the MLD in month N. Blue lines are for 16 individual members from the CFS, black lines for ensemble means, and red lines for observations (R2 and GODAS).

Fig. 10. Seasonal variations of area-averaged (20^{o}–65^{o}N, 125^{o}E–120^{o}W) monthly mean variance of (a) surface latent heat flux (LHTFL), (b) surface sensible heat flux (SHTFL), (c) surface net long wave radiation flux (LWRF; blue) and short wave radiation flux (SWRF; green), and (d) heat flux due to Ekman transport associated with the PDO in the CFS (blue) and R2 (red). The results are obtained by regressing flux anomalies against the PC time series of the first EOF of North Pacific SST in individual 30-yr segments. Blue and green lines are for 16 individual members from the CFS and black lines for ensemble means.

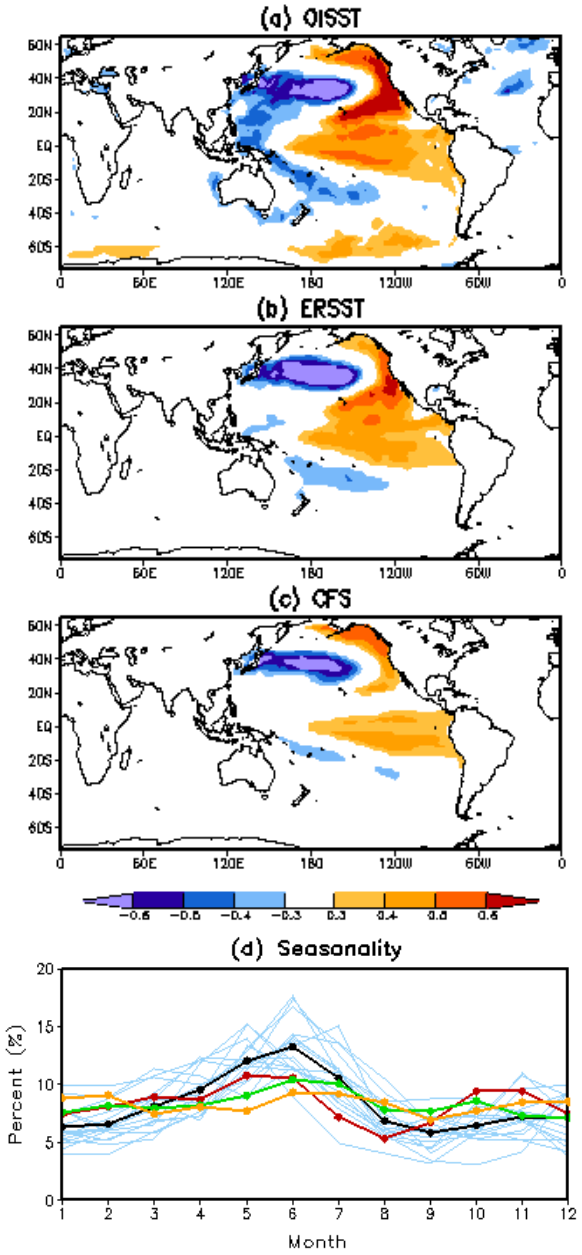

Fig. 1. Spatial patterns of SST associated with the first EOF of monthly mean SST over the North Pacific (20°N–65°N, 125°E–100°W) based on the (a) OISST data during 1982–2010, (b) ERSST during 1861–2010, and (c) the ensemble average of 16 leading EOFs for individual 30-yr segments from the 480-year CFS coupled run, and (d) seasonal distribution of the percentage variance of PC time series with red for the OISST, green for the ERSST, orange for the PDO index (1900–2010; Mantua et al. 1997), light blue for 16 individual 30-yr segments, and black for the 16-member ensemble. The spatial patterns in (a,b,c) are displayed in correlation maps in which the monthly mean SST anomalies at each grid point are correlated with the corresponding PC time series.

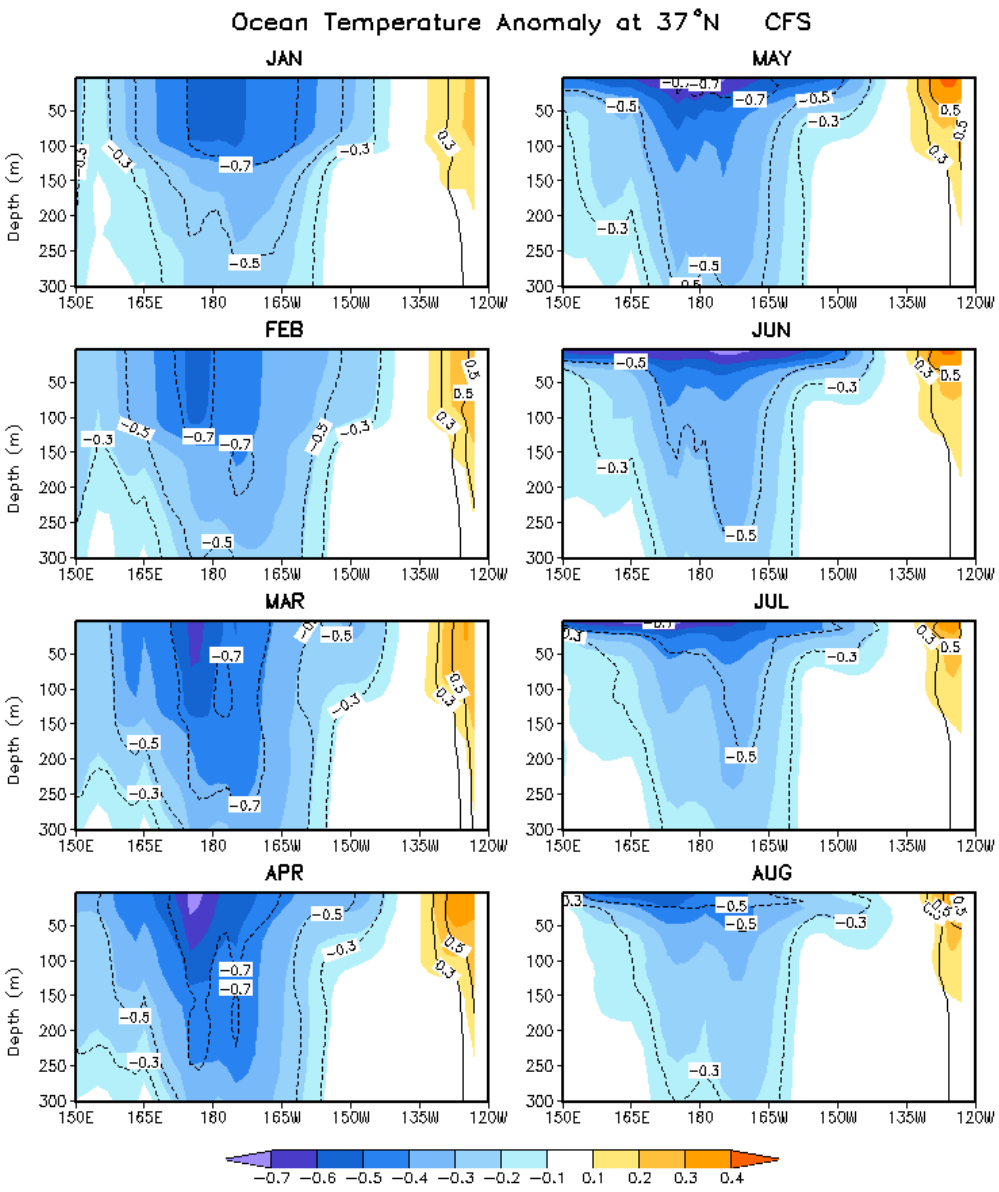

Fig. 2. PDO-related monthly ocean temperature anomalies (shading, ^{o}C) and correlation (contour) with the PDO PC time series at 37^{o}N across the North Pacific in the CFS. The anomalies are obtained by regressing ocean temperature anomaly vs. the PC time series of the first EOF of North Pacific SST in individual 30-yr segments. The anomalies are based on the ensemble average of 16 members and are associated with one standard deviation fluctuations in the PC time series for months from January to August. The correlation coefficients are also based on the ensemble average of the 16 members. Contours are ±0.3, ±0.5, and ±0.7 with negative contours dashed.

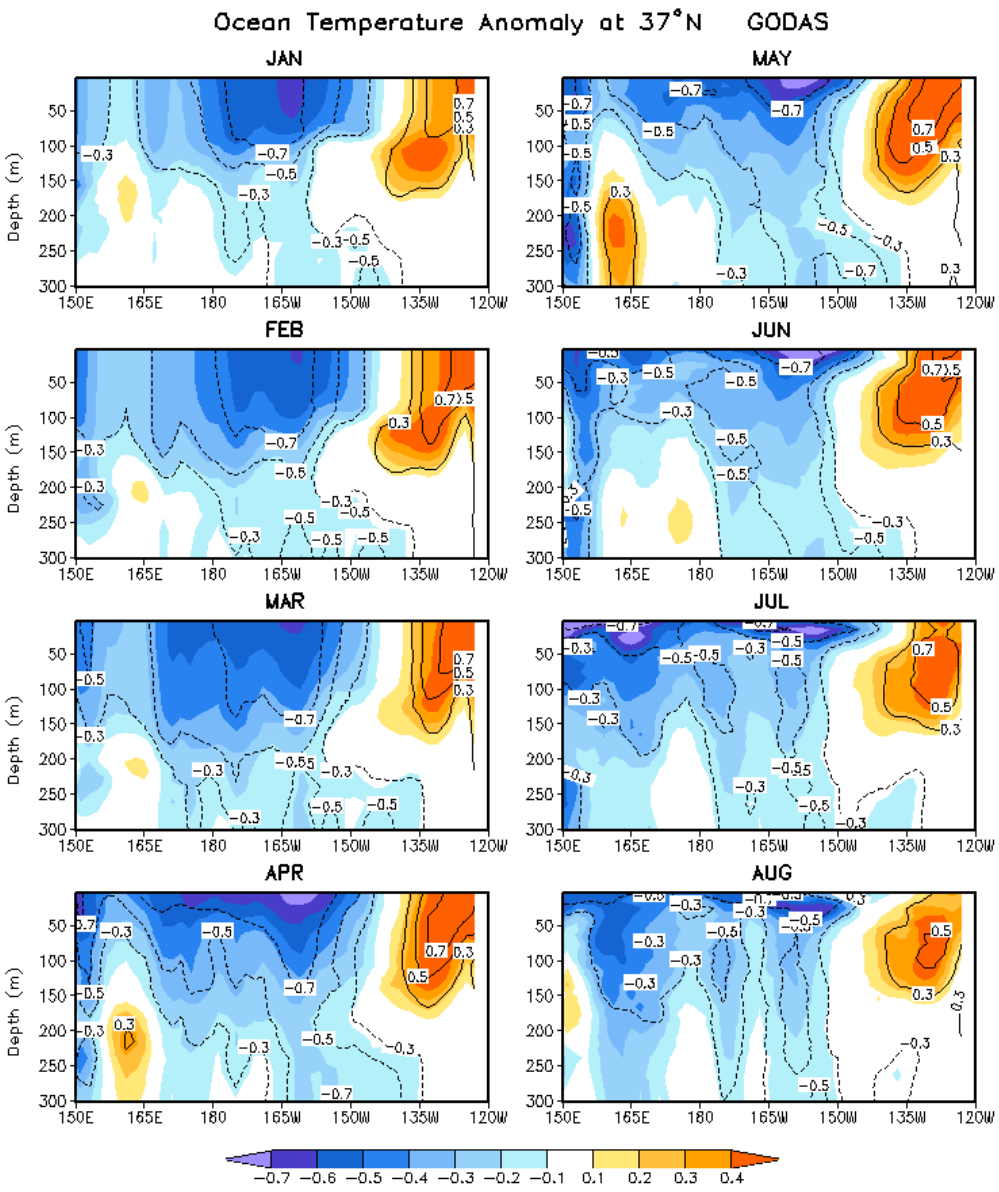

Fig. 3. Same as in Fig. 2, but based on 29-yr (1982–2010) ocean temperature from the GODAS and the first EOF of North Pacific SST from the OISST.

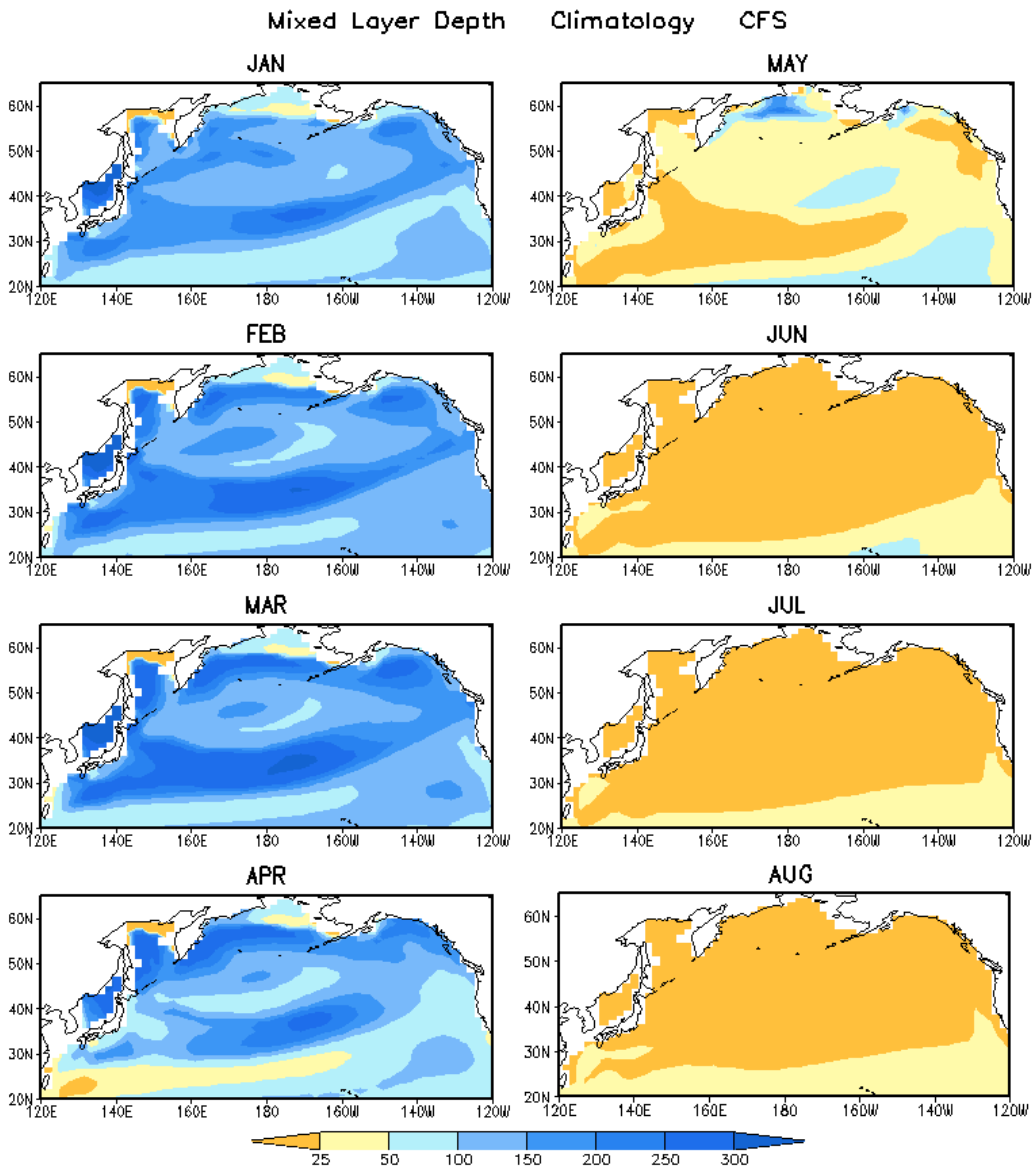

Fig. 4. Monthly climatology of the mixed layer depth (MLD; m) in the North Pacific derived from the CFS coupled run ensemble averaged over 16 30-yr segments for months from January to August.

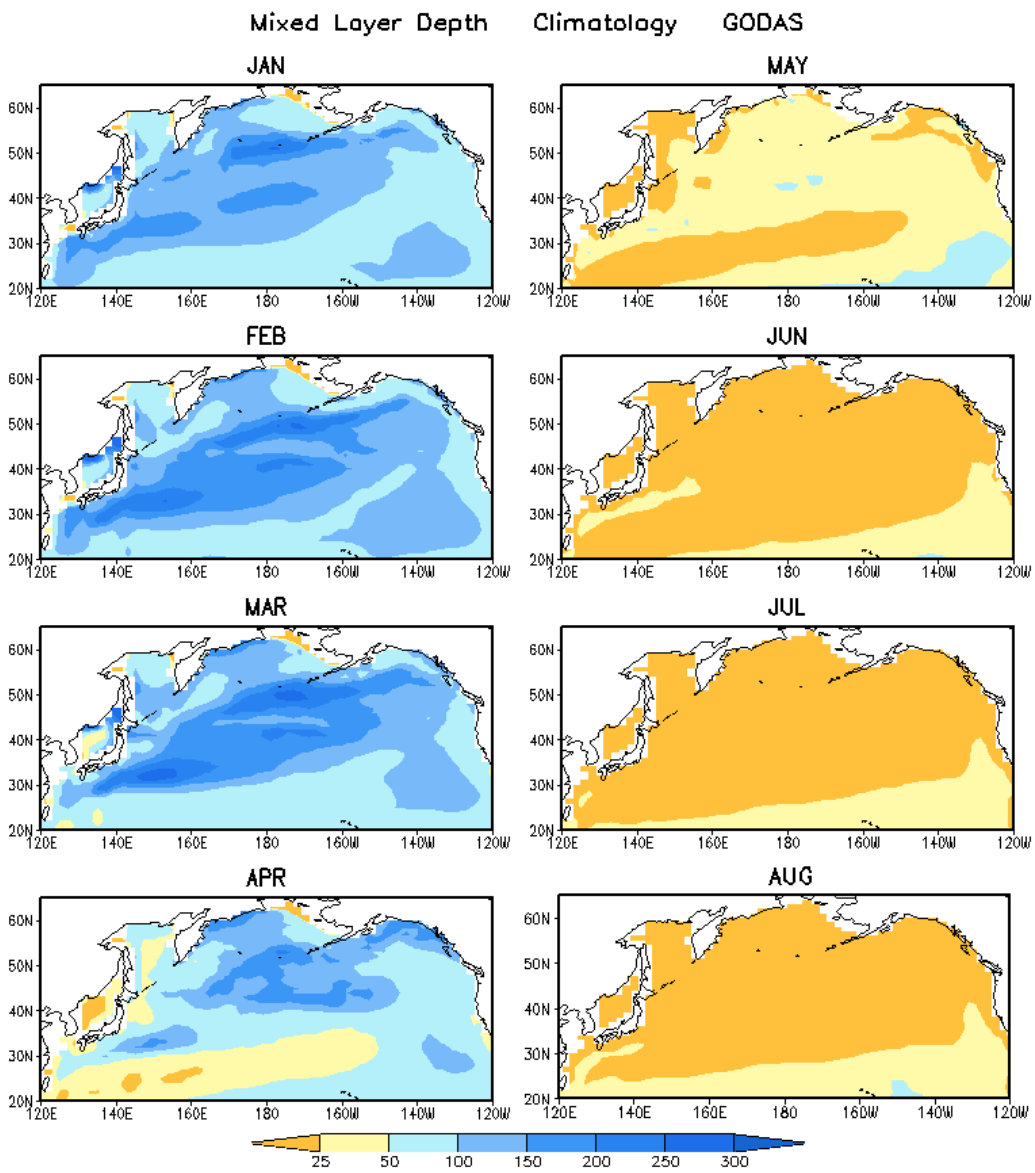

Fig. 5. Same as in Fig. 4, but based on 29-yr (1982 – 2010) GODAS data.

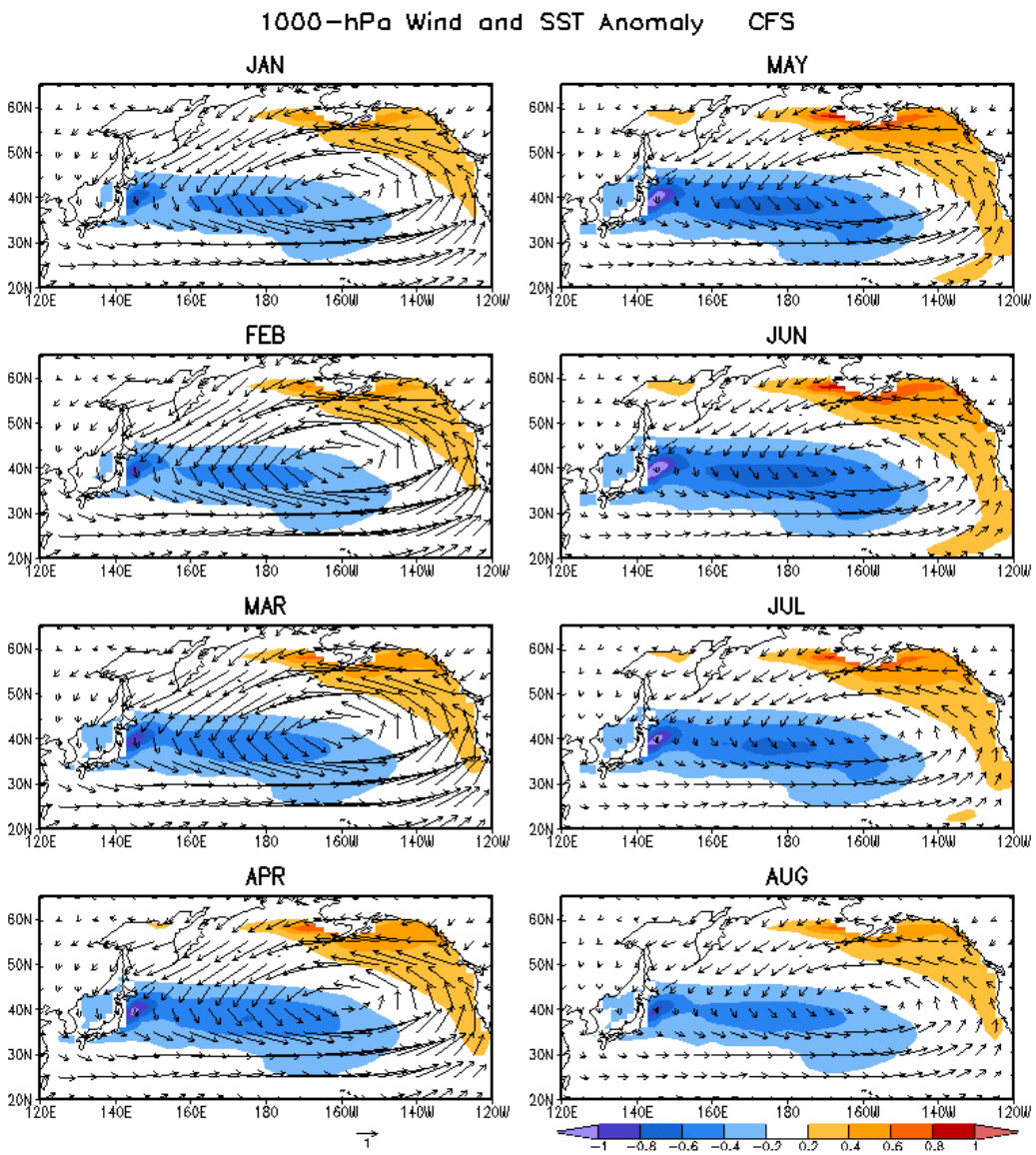

Fig. 6. Regression patterns of 1000-hPa wind (vectors; m s^{-1}) and SST (shadings, ^{o}C) anomalies in the CFS associated with one standard deviation departures of the PC time series of the first EOF of 1000-hPa zonal wind and SST anomalies over the North Pacific, respectively. The regressions are performed over the 30-yr period and all months, but one standard deviation values of the PC time series are calculated for individual months from January to August. The results are shown based on 16-member ensemble.

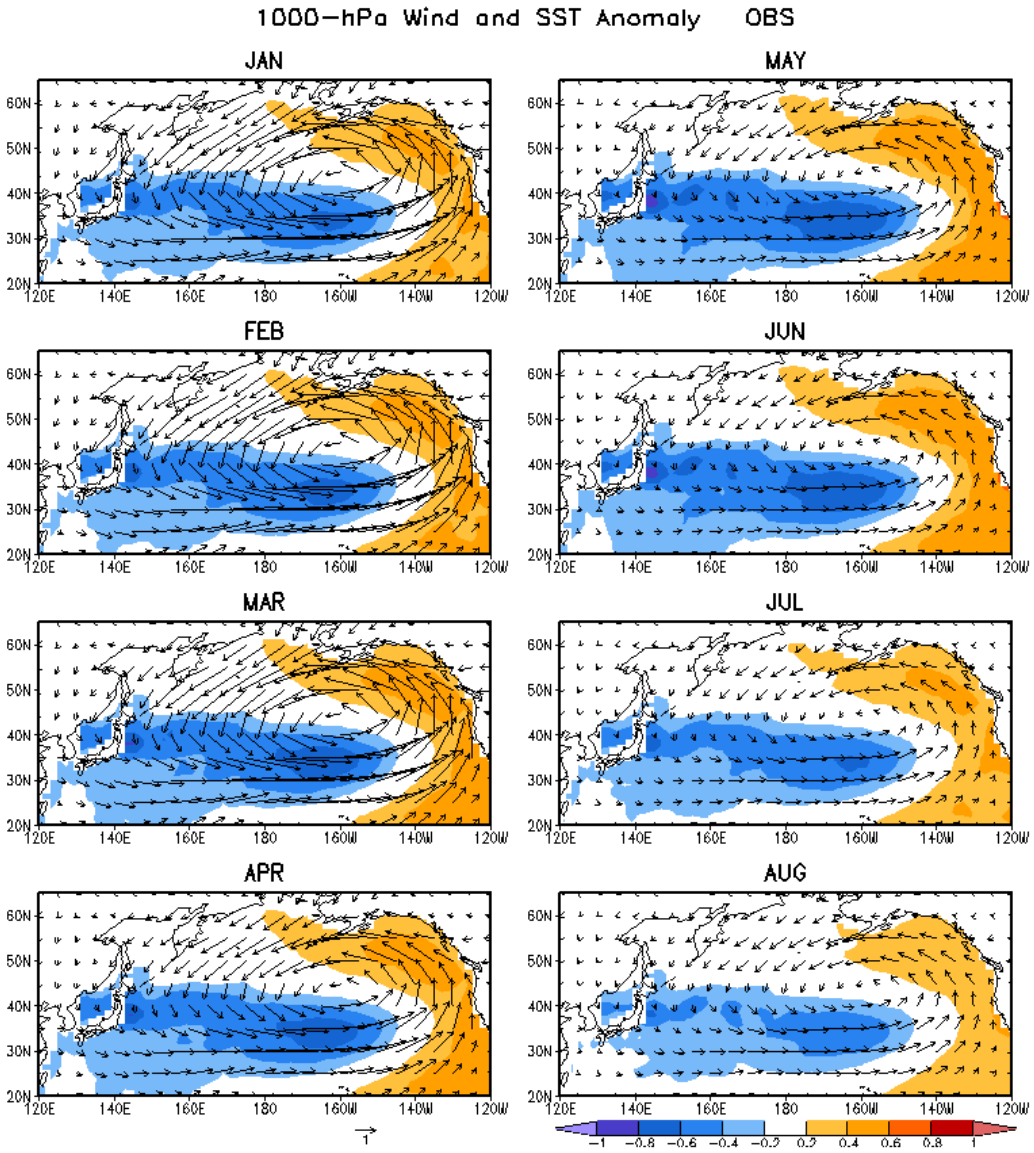

Fig. 7. Same as in Fig. 6, but based on 29-yr (1982 – 2010) 1000-hPa wind from R2 and OISST.

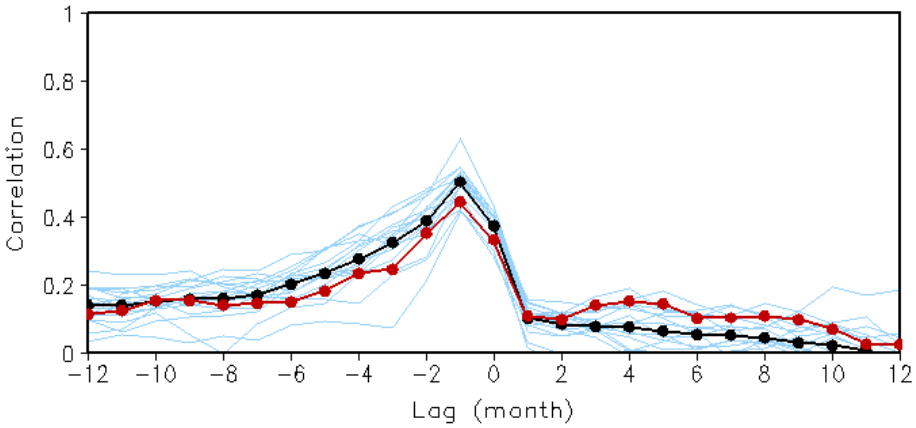

Fig. 8. Lag correlations between the PC time series of the first EOF of monthly 1000-hPa zonal wind and SST over the North Pacific in the CFS coupled run for each 30-yr period (light blue) and ensemble average (black) of the 16 correlation coefficients at different lags and those using 29-yr 1000-hPa zoanl wind from R2 and OISST (red). Negative (positive) lag means the 1000-hPa zonal wind leading (lagging) the SST.

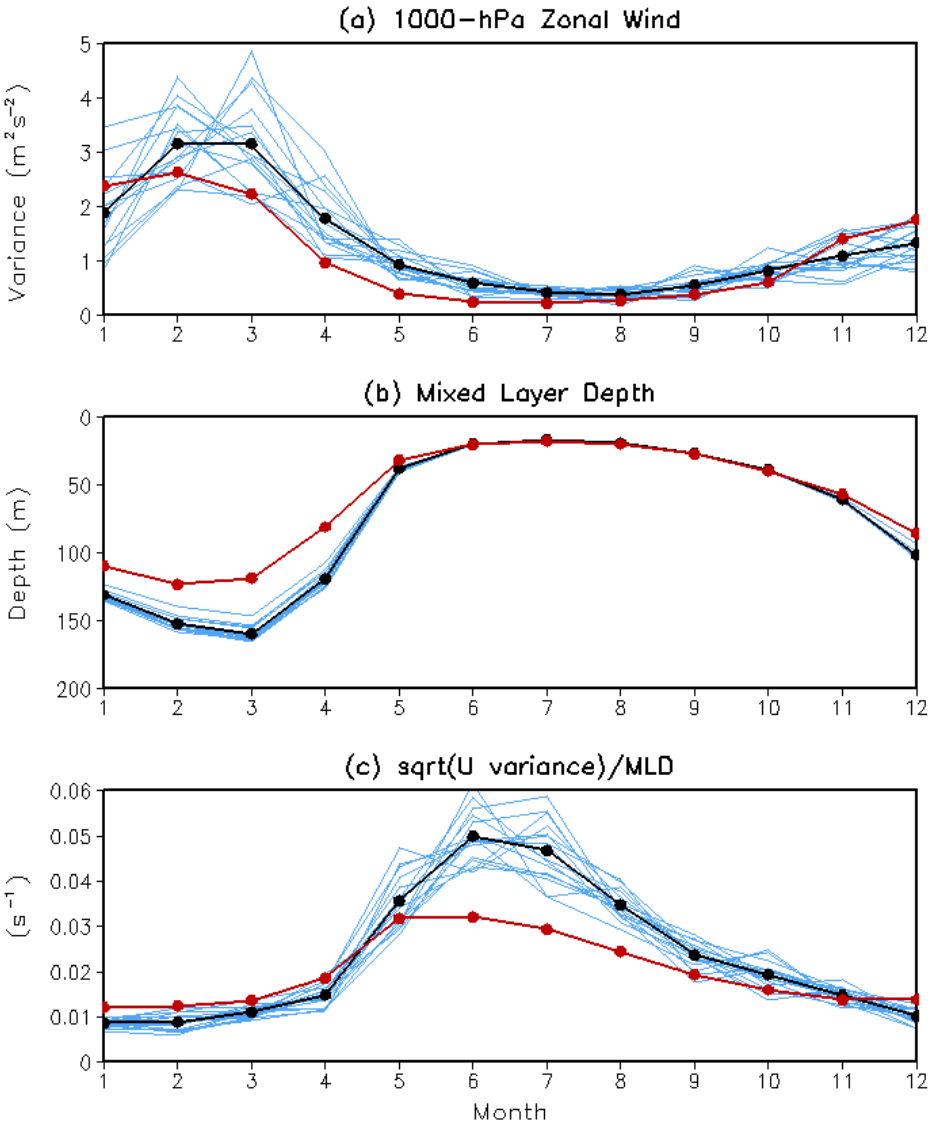

Fig. 9. Seasonal variations of area-averaged (20°–65°N, 125°E–120°W) (a) monthly mean variance of the 1000-hPa zonal wind anomaly associated with the first EOF, (b) climatological MLD, and (c) square root of the zonal wind variance in month N–1 divided by the MLD in month N. Blue lines are for 16 individual members from the CFS, black lines for ensemble means, and red lines for observations (R2 and GODAS).

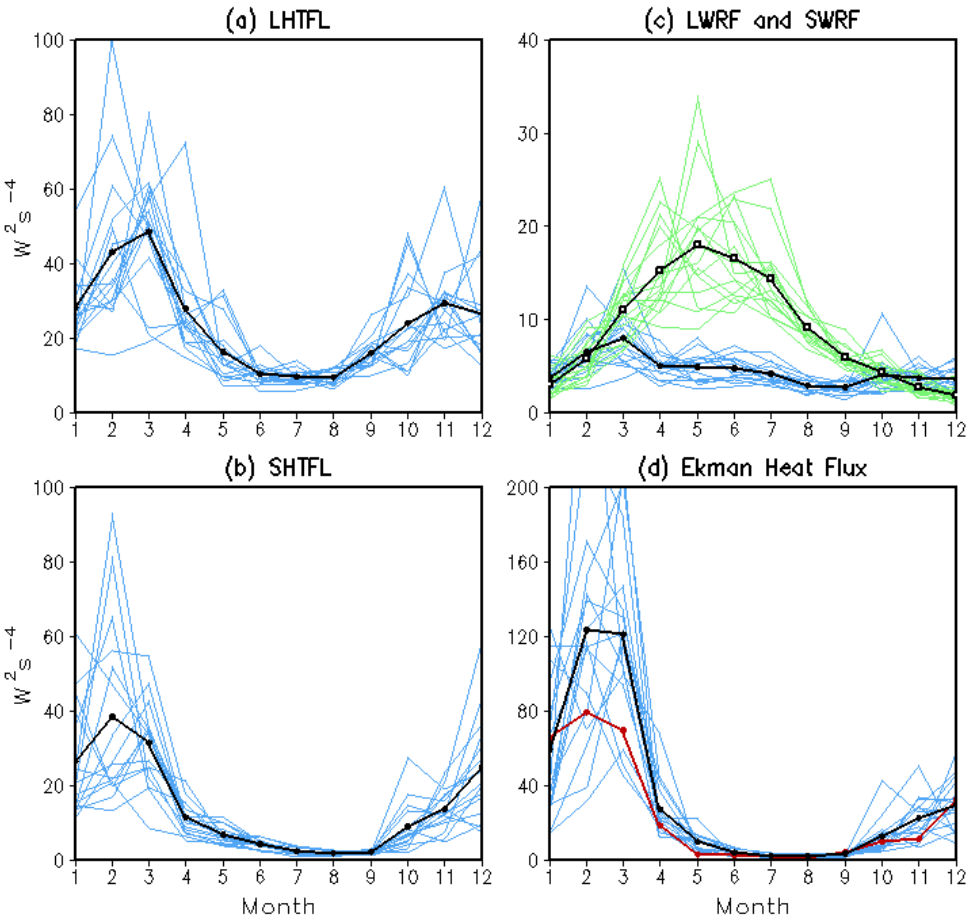

Fig. 10. Seasonal variations of area-averaged (20°–65°N, 125°E–120°W) monthly mean variance of (a) surface latent heat flux (LHTFL), (b) surface sensible heat flux (SHTFL), (c) surface net long wave radiation flux (LWRF; blue) and short wave radiation flux (SWRF; green), and (d) heat flux due to Ekman transport associated with the PDO in the CFS (blue) and R2 (red). The results are obtained by regressing flux anomalies against the PC time series of the first EOF of North Pacific SST in individual 30-yr segments. Blue and green lines are for 16 individual members from the CFS and black lines for ensemble means.